

A novel deep learning method for large-scale analysis of bone marrow adiposity using UK Biobank Dixon MRI data

David M Morris^{1,2,#}, Chengjia Wang^{1,3,#}, Giorgos Papanastasiou^{2,4}, Calum D Gray², Sammy Badr^{5,6}, Julien Paccou^{5,7}, Scott IK Semple^{1,2}, Tom MacGillivray⁸, and William P Cawthorn^{1*}

¹University/BHF Centre for Cardiovascular Science, University of Edinburgh, The Queen's Medical Research Institute, Edinburgh BioQuarter, 47 Little France Crescent, Edinburgh, EH16 4TJ, UK. ²Edinburgh Imaging, University of Edinburgh, The Queen's Medical Research Institute, Edinburgh BioQuarter, 47 Little France Crescent, Edinburgh, EH16 4TJ, UK. ³School of Mathematics and Computer Sciences, Heriot-Watt University, Edinburgh, EH14 1AS, UK. ⁴School of Computer Science and Electronic Engineering, Wivenhoe Park, The University of Essex, Colchester, CO4 3SQ, UK. ⁵University of Lille, Marrow Adiposity and Bone Laboratory (MABlab) ULR 4490, F-59000 Lille, France. ⁶CHU Lille, Department of Radiology and Musculoskeletal Imaging, F-59000 Lille, France. ⁷CHU Lille, Department of Rheumatology, F-59000 Lille, France. ⁸Centre for Clinical Brain Sciences, University of Edinburgh, The Queen's Medical Research Institute, Edinburgh BioQuarter, 47 Little France Crescent, Edinburgh, EH16 4TJ, UK.

#These authors contributed equally to this work.

***Correspondence to:** William Cawthorn, University/BHF Centre for Cardiovascular Science, The Queen's Medical Research Institute, Edinburgh BioQuarter, 47 Little France Crescent, Edinburgh, EH16 4TJ.

Email: W.Cawthorn@ed.ac.uk

Tel: +44(0)1312426691

Fax: +44(0)1312426779

Short title: Deep learning for marrow fat in the UK Biobank

Key words: Deep learning; Bone marrow adiposity; Magnetic resonance imaging; UK Biobank; Bone; Biomarkers

Highlights:

- We establish a new deep learning method for image segmentation.
- Our method improves segmentation of small structures from large volumetric data.
- Using our method, we assess bone marrow fat fraction (BMFF) in UK Biobank MRI data.
- This is the first use of deep learning for large-scale, multi-site BMFF analysis.
- Our results highlight the potential of BMFF as a new clinical biomarker.

42 **ABSTRACT**

43

44 **OBJECTIVES:** Bone marrow adipose tissue (BMAT) represents >10% of total fat mass
45 in healthy humans and further increases in diverse clinical conditions, but the impact
46 of BMAT on human health and disease remains poorly understood. Magnetic
47 resonance imaging (MRI) allows non-invasive measurement of the bone marrow fat
48 fraction (BMFF), and human MRI studies have begun identifying associations between
49 BMFF and skeletal or metabolic diseases. However, such studies have so far been
50 limited to smaller cohorts: analysis of BMFF on a larger, population scale therefore
51 has huge potential to reveal fundamental new knowledge of BMAT's formation and
52 pathophysiological functions. The UK Biobank (UKBB) is undertaking whole-body MRI
53 of 100,000 participants, providing the ideal opportunity for such advances.

54

55 **MATERIALS AND METHODS:** Herein, we developed a deep learning pipeline for
56 high-throughput BMFF analysis of these UKBB MRI data. Automatic bone marrow
57 segmentation was achieved by designing new lightweight attention-based 3D U-Net
58 convolutional neural networks that allowed more-accurate segmentation of small
59 structures from large volumetric data. Using manual segmentations from 61-64
60 subjects, the models were trained against four bone marrow regions of interest: the
61 spine, femoral head, total hip and femoral diaphysis. Models were validated using a
62 further 10-12 datasets for each region and then used to segment datasets from a
63 further 729 UKBB participants. BMFF was then determined and assessed for expected
64 and new pathophysiological characteristics.

65

66 **RESULTS:** Dice scores confirmed the accuracy of the models, which matched or
67 exceeded that for conventional U-Net models. The BMFF measurements from the
68 729-subject cohort confirmed previously reported relationships between BMFF and
69 age, sex and bone mineral density, while also identifying new site- and sex-specific
70 BMFF characteristics.

71

72 **CONCLUSIONS:** We have established a new deep learning method for accurate
73 segmentation of small structures from large volumetric data. This method works well
74 for accurate, large-scale BMFF analysis from UKBB MRI data and has the potential to
75 reveal novel clinical insights. The application of our method across the full UKBB
76 imaging cohort will therefore allow identification of the genetic and pathophysiological
77 factors associated with altered BMAT. Together, our findings establish the utility of
78 deep learning for population-level BMFF analysis and promise to help elucidate the
79 full impact of BMAT on human health and disease.

80 1. INTRODUCTION

81 Bone marrow adipose tissue (BMAT) accounts for up to 70% of total bone marrow
82 (BM) volume and approximately 10% of total fat mass in lean, healthy humans (1).
83 BMAT further increases with ageing and in diverse clinical conditions, including
84 osteoporosis, obesity, type 2 diabetes, oestrogen deficiency, chronic kidney disease,
85 radiotherapy and glucocorticoid treatment (1). In striking contrast to other adipose
86 depots, BMAT also increases during caloric restriction in animals and in humans with
87 anorexia nervosa (1-4). Thus, BMAT is a major component of normal human anatomy;
88 is distinct to other types of adipose tissue; and is altered in numerous clinical contexts.

89 These observations suggest roles for BMAT in normal physiological function and
90 the pathogenesis of multi-morbidities, including major ageing-associated diseases.
91 Indeed, clinical and preclinical studies suggest that BMAT can directly influence
92 skeletal remodelling, haematopoiesis and energy homeostasis (1, 5, 6) and have
93 revealed endocrine properties through which BMAT may exert systemic effects (3).
94 However, study of BMAT has been limited, especially in comparison to other major
95 adipose depots (1); hence, BMAT formation and function remains poorly understood.

96 Despite this relative ignorance, recent studies have revealed new fundamental
97 knowledge of BMAT biology. One key finding is that BMAT's characteristics and
98 functions differ according to its skeletal location. BMAT is proposed to exist in two
99 broad subtypes, dubbed 'constitutive' and 'regulated' (7, 8): constitutive BMAT
100 predominates in the appendicular skeleton, particularly at more-distal sites, whereas
101 regulated BMAT develops in the axial skeleton and in proximal regions of the long
102 bones, such as the femoral head and epiphysis. Adipocytes within regulated BMAT
103 increase or decrease in size and/or number in response to altered environmental,
104 physiological and pathological conditions, whereas those within constitutive BMAT are
105 relatively resistant to expansion or breakdown in such contexts (7, 8). Thus, efforts to
106 further elucidate BMAT formation and function must consider these fundamental site-
107 specific differences.

108 Magnetic resonance imaging (MRI) and proton MR spectroscopy have emerged
109 as key tools for non-invasively assessing BMAT properties in humans (9), including
110 the extent of BM adiposity and the proportions of saturated and unsaturated lipids
111 within the BM (10). The former depends on analysis of BM fat fraction (BMFF) using
112 chemical shift-encoding based water-fat separation methods. These approaches have
113 been applied in various small- and mid-scale human cohort studies, revealing some
114 insights into BMAT's association with human skeletal and metabolic health (11, 12).
115 For example, multiple studies have shown that BMFF is increased in osteoporosis and
116 is associated with lower bone mineral density (BMD) in non-osteoporotic subjects (11-
117 13). However, these cohort studies have never included more than 560 people (13),
118 limiting the ability to detect other associations. Thus, analysis of BMFF on a larger
119 scale has enormous potential to reveal fundamental new knowledge of BMAT
120 formation and function, including the association with other physiological, pathological
121 and genetic variables. This would provide new understanding about the factors that
122 regulate BMAT development, as well as highlighting how altered BMFF impacts
123 human health and disease.

124 The UK Biobank (UKBB) is undertaking the world's largest health imaging study
125 (14), providing an ideal opportunity for such large-scale BMFF analysis. Of the
126 500,000 UKBB participants, 100,000 are undergoing MRI of the brain, heart and whole
127 body, as well as dual-energy X-ray absorptiometry to measure BMD. As of August
128 2022, approximately 53,000 participants have been scanned. Efficient measurement
129 of BMFF from these MRI datasets will require development of new automated analysis

130 methods. Several groups have developed machine learning for automated
131 segmentation of other anatomical regions from the UKBB MRI data (15-17). Machine
132 learning has also recently been used to segment the knee or vertebral BM from Dixon
133 images in smaller cohorts outwith the UKBB (18-20); however, machine learning has
134 not yet been developed for automated segmentation of the BM from other skeletal
135 sites, and never using MR data from the UKBB. These were the goals of the present
136 study.

137 Given the potential insights that could be gained from such large-scale BMFF
138 analysis, herein we developed a deep learning pipeline for automated BM
139 segmentation from UKBB MRI data. Our findings establish the utility of deep learning
140 for large-scale analysis of BMFF within the UKBB and the potential of this approach
141 for revealing the impact of BMAT on human health and disease.

142 **2. MATERIALS AND METHODS**

143 **2.1. UKBB Imaging study – participants**

144 Full details of the UKBB imaging study have recently been reported by Littlejohns *et*
145 *al*, who summarise the study as "*a population-based cohort of half a million*
146 *participants aged 40–69 years recruited between 2006 and 2010. In 2014, UK Biobank*
147 *started the world’s largest multi-modal imaging study, with the aim of re-inviting*
148 *100,000 participants to undergo brain, cardiac and abdominal magnetic resonance*
149 *imaging, dual-energy X-ray absorptiometry and carotid ultrasound*" (14). As of August
150 2022, over 53,000 participants have undergone the UKBB imaging protocol. The
151 phenotypic and imaging data used in this study were obtained from UKBB and
152 analysed under an approved project application (ID 48697). All work reported herein
153 was done in accordance with UKBB ethical requirements.

154

155 **2.2. UKBB – MRI acquisition**

156 MRI data were acquired on a 1.5 T whole-body MR system (Magnetom Aera, Siemens
157 Medical Solutions, Erlangen, Germany). Tridimensional two-point Dixon sequences
158 were used to give coverage from neck to knees, consisting of six volumes. In the
159 present study we analysed three of these volumes: the abdomen, hips, and upper leg.
160 For the abdomen and hips, breath-hold sequences were acquired by using a 3D dual-
161 echo spoiled gradient-echo (FLASH) T1-weighted acquisition using the following
162 parameters: TR/TE_{in-phase}/TE_{out-of-phase}: 6.7/4.8/2.4 ms; field of view (FOV): 500 x 381
163 mm; slice thickness: 4.5 mm; isotropic in-plane spatial resolution of 2.2 mm; number
164 of slices: 44. Parallel imaging factor 2 in both frequency/phase directions and a partial
165 Fourier reconstruction of 71% were used to reduce acquisition time. For the upper leg
166 slice, slice thickness was reduced to 3.5 mm and 72 slices were acquired with the
167 same resolution. Detailed technical parameters are available in the UKBB rationale
168 (14).

169

170 **2.3. UKBB – DXA scans for bone mineral density measurement and body** 171 **composition**

172 As part of the UKBB Imaging study, bone mineral density (BMD) was measured at the
173 lumbar spine (L1–L4) and at the non-dominant hip for femoral neck and total hip by
174 DXA scan (GE-Lunar iDXA). Machines were calibrated daily, and quality-assurance
175 tests were carried out periodically. WHO criteria were used to define osteoporosis
176 (BMD T-score ≤ -2.5) and osteopenia (BMD T-score between -1.0 and -2.5). All
177 UKBB imaging participants also underwent total-body DXA scanning (GE-Lunar
178 iDXA). Fat, lean, and bone masses for the total body and per region (arms, legs, and
179 trunk) were measured and analyzed using the manufacturer’s validated software, with
180 visceral adipose tissue (VAT, kg) also measured. Daily quality-control and calibration
181 procedures were performed using the manufacturer’s standards.

182

183 **2.4. Training and validation cohort**

184 To develop a deep learning method for automated BM segmentation we focussed on
185 a subset of UKBB Imaging participants, consisting of 729 male and female subjects
186 aged 60-69 years old (Table 1). This cohort was selected to include control subjects
187 (with normal BMD) and subjects with osteopaenia or osteoporosis. Subjects with
188 obesity and type 2 diabetes were excluded because these conditions can influence
189 BMFF (1, 6), leaving only non-diabetic subjects with a body mass index (BMI) within
190 the normal range (18.5-25 kg/m²).

191

192 **2.5. Data management and workflow**

193 MRI data was downloaded from UKBB, consisting of multiple volumes acquired using
194 the 2-point Dixon technique, based on the parameters listed above. For each volume
195 the in- and out-of-phase, fat and water images were available. The data were
196 downloaded in flat format and sorted by sequence to expedite data access. The
197 volumes required were identified by their sequence number assuming a standard
198 acquisition protocol, which was determined from the data. As shown in Figure 1, we
199 began by downloading and analysing data from the 729-subject training and validation
200 cohort.

201 **2.6. Manual segmentation of MRI data**

202 A training dataset of 75 subjects (Fig. 1A) was extracted from the test dataset to be
203 used for the training and validation of the deep learning algorithms. Each of these 75
204 datasets was segmented by a single observer for consistency, generating manual
205 segmentations. For each subject, the fat images were used to define four distinct
206 volumes of interest (VOIs) corresponding to BM regions of pathophysiological
207 relevance: the spine, the femoral head, the total hip, and the femoral diaphysis. The
208 spine consisted of all the vertebral marrow in the principle abdominal volume, which
209 contained 6-7 vertebrae ranging from T8 to L3. The reason for this range of vertebrae
210 is that the multiple abdominal acquisitions have a fixed volume and are continuous
211 across the patient's body; hence, the range of vertebrae within each abdominal volume
212 depends on the patient's height. The femoral head and total hip regions were
213 segmented from the hip volume. Here, the total hip consisted of the femoral neck and
214 the hip between the lesser and greater trochanter. The femoral diaphysis, located in
215 the upper leg volume, was segmented at the mid-shaft of the femur, which was
216 identified by locating the point of the shaft with the narrowest cross section. Each
217 femoral volume was segmented from the non-dominant left femur to allow more-direct
218 comparison with DXA measurements, which are usually performed at the non-
219 dominant hip. Femoral BMFF does not show significant contralateral differences (21),
220 meaning that BMFF measurements from the left femur should be representative of
221 both sides. Segmentation was performed on the native axial images on a slice-by-slice
222 basis in Analyze 12.0 software (AnalyzeDirect, Overland Park, KS, USA) following an
223 overall inspection of each volume to determine the extent of each region excluding
224 partial volume, defined as a drop in signal intensity > 50% compared to the centre of
225 the region.

226
227 Of the 75 manually segmented datasets (Fig. 1A), 64 were used to train the deep
228 learning model for the spine; 61 were used for the femoral head and diaphysis; and
229 62 were used for the total hip (Fig. 1B). To do so, the fat images and their
230 corresponding manual segmentations were used iteratively to build a separate model
231 to segment each region individually and generate a deep learning segmentation (Fig.
232 1D). The remaining datasets (Fig. 1C) were not used in training the models but instead
233 were used as unseen validation data to test the models: 12 datasets were used for
234 testing the spine, 11 for the femoral head, and 10 each for the total hip and diaphysis
235 models. For these validation datasets, comparison of the deep learning segmentations
236 with the manual segmentations (Fig. 1E) allowed dice coefficients to be calculated for
237 the four different algorithms (Table 2).

238
239 All the deep learning segmentations for the training and validation datasets were
240 manually checked. This identified several data issues and segmentation failures that
241

242 required the development of specific error-checking rules. These rules were based on
243 determining if the VOIs generated were physiologically appropriate: VOIs could not
244 consist only of single voxels, nor were gaps allowed within the VOIs. Therefore, the
245 initial error-checking steps automatically removed any single-voxel VOIs and joined
246 together any discontinuous VOIs. Additional error checking was used to identify those
247 segmentations that were outliers within the distribution of regions generated. This was
248 based on the centre of mass being greater than 3 standard deviations from the mean
249 of the training dataset. This is useful for identifying erroneous segmentations that have
250 been caused by data quality issues or deviations from the standard MRI protocol.

251

252 **2.7. U-Net design and rationale**

253 Directly segmenting 3D data using a traditional U-Net (22) has several drawbacks: i),
254 the size of input data and the depth of the model are limited by the available GPU
255 memory; ii), due to the highly imbalanced distribution between classes, the traditional
256 3D U-Net (22) tends to label all voxels as background; and iii), the fixed size of the
257 receptive field limited the ability of the model to effectively utilize the global correlations
258 between local features.

259

260 To address these issues, we developed a novel light-weight attention-based U-Net
261 model for simultaneous detection and segmentation of tiny structures in large 3D data.
262 Figure 2 shows the architecture of this new Attention ROI U-Net model. The encoding
263 subnetwork output feature maps four resolution levels (23). Each encoding block
264 consists of a conventional U-Net convolutional layer (3D conv + Relu + Instance
265 normalization), a convolutional layer equipped with a modified convolutional block
266 attention module (CBAM) (24), and a down-sampling layer implemented as a stride 2
267 3X3X3 convolution operation. The last encoding block consists of two CBAM
268 convolutional layers with a non-local spatial attention layer (25) inserted between
269 them. Unlike the original CBAM, which generates two attention maps using average
270 and max pooling, we used 1X1X1 convolution to generate one single fixed-size
271 attention map from each CBAM layer. The 5 attention maps are all resized to
272 96X96X96 and then fused by a mini convolutional neural network (CNN) with a
273 *Softmax* layer to generate a probability map \mathbf{P} . The centre, $(x, y, z)_{ROI}$, of a region of
274 interest (ROI), which indicates the location of the segmented anatomical structure, is
275 then given by:

$$276 \quad (x, y, z)_{ROI} = \mathbf{P} \odot (\mathbf{u}, \mathbf{v}, \mathbf{w}),$$

277 Here, $\mathbf{u}, \mathbf{v}, \mathbf{w}$ are grid of data coordinates normalized to [-1, 1]. With this centre, a cubic
278 ROI is extracted from the encoder feature maps of all resolution levels with sizes 32,
279 16, 8 and 4. The U-Net decoder then generates the segmentation of this ROI. The
280 final segmentation results are produced by recovering the ROI location within the
281 original data volume.

282

283 Detection of the ROI location is realised by minimizing a ROI centre localization loss,
284 L_{loc} , defined on the predicted and ground-truth ROI centres. We use the conventional
285 Dice loss, L_{ROI} , to optimize the segmentation of the detected ROI. Because minimize
286 bias in traduced by the class imbalance on the final segmentation results, we also
287 compute a weighted Dice loss, L_{seg} , using the full image segmentation, where the
288 weight of each class is defined as the reciprocal of the number of voxels. To sum up,
289 the loss function for trains ing our new U-Net model is defined as:

$$290 \quad L = L_{seg} + \lambda_1 L_{ROI} + \lambda_2 L_{loc},$$

291 where λ_1 and λ_2 control the weights between different losses. In this work, we set
292 $\lambda_1 = \lambda_2 = 1$. The proposed algorithm was implemented in Pytorch (26) with an Adam
293 optimizer (27).

294

295 **2.8. Fat fraction mapping**

296 Fat fraction (FF) measurements from MRI data allow for the determination of the
297 relative quantities of water and fat present within tissue, based on the different
298 resonant frequencies of hydrogen atoms bound to fat and water. Acquisition of in- and
299 out-of-phase images allows fat and water images to be generated. Based on the
300 intensities of these images the FF was calculated as a percent of the voxel volume.
301 This was done for all volumes of interest. The specific VOIs, segmented using our
302 novel U-Net model, were then applied to the FF maps to allow extraction of the FF for
303 each VOI. This used the fat and water images for each volume of interest and nearest-
304 neighbour smoothing was applied to the images before the maps were calculated to
305 minimise the influence of any noise spikes in the data. In house code (Matlab 2019B,
306 The Mathworks Inc, Natick, Massachusetts, USA) applied the deep learning
307 segmentations to the FF maps after erosion of the spine, head and total hip regions
308 by a single boundary voxel in plane to ensure measurements were from marrow and
309 not bone. This erosion step was not applied to the diaphysis segmentations because
310 of the small cross section of this region (for some patients the diaphyseal cross section
311 is so small that it would be eliminated by the erosion step).

312

313 **2.9. Data presentation and statistical analysis**

314 Data were analysed for normal distribution using the Anderson-Darling test. For results
315 tables of summary statistics, normally distributed data are reported as mean \pm SEM
316 and were compared using one-way or two-way ANOVA with Šídák's test for multiple
317 comparisons. Non-normally distributed data are reported as median [interquartile
318 range] and were compared using the Kruskal-Wallis test, with Dunn's test for multiple
319 comparisons; the latter was also used when comparing normally distributed data with
320 non-normally distributed data. Images of manual and deep learning segmentations
321 were generated using 3DSlicer (v4.11) and colours adjusted using GIMP2. Graphs of
322 summary data are presented as Violin plots overlaid with individual data points.
323 Visualisation and statistical analysis of these summary data were done using Prism
324 software (v9.4.1, GraphPad, USA). Univariable regression analyses were done in
325 RStudio v2022.02.1 (Build 461), with multivariable regression performed using finalfit
326 (R package v1.0.5) (28). Subjects with any erroneous measurements (e.g. a BMD of
327 0 g/cm²) were excluded from the regression analyses. A Bonferroni-adjusted *P*-value
328 <0.05 was considered statistically significant.

329

330 **2.10. Data and code availability**

331 All data for FF and segmentation volumes will be uploaded to the UKBB. Code for the
332 deep learning models will be made available via GitHub. Code for regression analyses
333 will be made available via DataShare (<https://datashare.ed.ac.uk>). Until these data are
334 publicly available, the authors will agree to all reasonable requests for code and data
335 sharing, in accordance with UKBB guidelines.

336

337 **3. RESULTS**

338 **3.1. U-Net development and training**

339 We first used MRI data from 61-64 subjects for manual segmentation of four VOIs: the
340 spine, consisting of lumbar and thoracic vertebrae; the femoral head; total hip; and
341 femoral diaphysis. We then trained separate U-Net models for each VOI and tested
342 their performance on 10-12 subjects in a validation dataset (Fig. 1). Figure 2 shows
343 the architecture of our new U-Net, while Table 2 shows the comparison Dice index
344 results between the conventional U-Net and our new U-Net models for each site.
345 Visual comparison of manual vs deep learning segmentations further confirmed the
346 accuracy of the outputs from each of our deep learning models (Fig. 3).

347 **3.2. Segmentation and Fat Fraction mapping of training and validation cohort**

349 To test if our U-Net models yield reliable BMFF results, we next applied them to FF
350 maps from a cohort of 729 UKBB participants (Table 1). This cohort was chosen to
351 include both males and females aged 60-69, comprising individuals with osteoporosis,
352 osteopaenia, or normal BMD. The rationale for this is as follows: first, BMFF increases
353 with age and, for humans aged 60-69, vertebral BMFF is expected to be greater in
354 females than in males (29, 30); second, BMFF is increased in osteoporosis and
355 negatively associated with BMD (1, 6, 12); and finally, BMFF is greater in the femur
356 than in the lumbar spine (1, 31). Thus, applying our U-Net models to analyse spinal
357 and femoral BMFF in this cohort allowed us to test if the resulting deep learning
358 segmentations yield BMFF values that show these expected associations with sex,
359 age, BMD, and anatomical site. If so, this would validate the accuracy of our new
360 models for high-throughput BM segmentation and BMFF analysis.

361
362 As shown in Figure 4, we found that BMFF in healthy control subjects significantly
363 differed across the five regions analysed. This was most obvious for the spine, where
364 BMFF was lower than in each femoral region. However, BMFF also differed between
365 each femoral region, being highest in the femoral head and then decreasing
366 progressively in the total hip ($P = 0.0012$ vs femoral head) and diaphysis ($P < 0.0001$
367 vs femoral head or total hip). There were also significant, region-dependent sex
368 differences: spinal BMFF was greater in females than in males, whereas males had
369 greater BMFF at each femoral site (Fig. 4).

370
371 To further understand the regional and sex differences in BMFF, we investigated if
372 BMFF at one site is associated with BMFF at the other sites. As shown in Table 3,
373 there were strong positive associations between BMFF at each femoral site, with the
374 relationship between total hip BMFF and diaphyseal BMFF being stronger in males
375 than in females. Spinal BMFF was not associated with diaphyseal BMFF; however, it
376 was positively associated with femoral head BMFF in females, and with total hip BMFF
377 in males and females; the latter relationship was also stronger in females than in males
378 (Table 3). Thus, BMFF at one site is generally positively associated with BMFF at other
379 sites, and this relationship differs between the sexes.

380 **3.3. Effect of osteopaenia or osteoporosis on BMFF at each site**

382 We next investigated the effect of osteopaenia or osteoporosis on BMFF at each site.
383 As shown in Figure 5, osteopaenic or osteoporotic females had higher BMFF than
384 control females at each site analysed. In males, osteopaenia was associated with
385 significantly increased BMFF at the total hip and femoral diaphysis, and total hip BMFF
386 was also greater osteoporotic vs control males (Fig. 5). However, unlike in females,

387 BMFF at the spine or femoral head did not differ between normal, osteopaenic and
388 osteoporotic males, while diaphyseal BMFF also did not differ between osteoporotic
389 and normal males (Fig. 5).
390

391 **3.4. Univariable associations between BMD, BMFF and other traits.**

392 The lack of increased BMFF in osteoporotic males was unexpected and may result
393 from the low numbers in this group (Table 1). Thus, we next used univariable
394 regression to determine if BMFF shows the expected inverse association with BMD at
395 each site, regardless of osteoporotic status. We also investigated which other
396 variables are associated with BMD at each site. As shown in Supplemental Table 1,
397 BMD and BMFF were inversely associated at the spine and this relationship did not
398 differ between the sexes. A similar relationship existed between spine BMD and legs
399 fat %. In contrast, spine BMD was positively associated with visceral adipose tissue
400 (VAT) mass, android fat %, trunk fat % and BMI, with the latter relationship being
401 stronger in males than in females. There was no significant relationship between spine
402 BMD and age, total fat % or gynoid fat %; however, females showed a trend for lower
403 spine BMD with increasing age.
404

405 Univariable regression analyses for BMD at the femoral neck, total hip and femoral
406 shaft are presented in Supplemental Tables 2, 3 and 4, respectively. For femoral neck
407 BMD we detected robust inverse associations with BMFF at the femoral head, total
408 hip and spine; the latter relationship was assessed to determine if spinal BMFF is a
409 useful predictor of BMD at the femoral neck, given the clinical significance of fractures
410 at this site. Notably, the relationship with femoral head BMFF showed strong sexual
411 dimorphism, occurring robustly in females while being absent in males. Femoral neck
412 BMD also showed an inverse relationship also with legs fat % and a positive
413 association with BMI; however, no significant associations occurred for the other
414 explanatory variables tested (Supplemental Table 2).
415

416 Similar relationships occurred for total hip BMD, including sex differences in the
417 association with femoral head BMFF; an inverse association with legs fat %; and a
418 positive association with BMI (Supplemental Table 3). Unlike for femoral neck BMD,
419 total hip BMD also showed a positive association with VAT mass.
420

421 As for these other sites, femoral shaft BMD was inversely associated with BMFF at
422 the femoral diaphysis while being positively associated with BMI. Weaker negative and
423 positive associations were noted for legs fat % and VAT mass, respectively, and none
424 of these relationships differed between the sexes (Supplemental Table 4).
425

426 **3.5. Univariable associations between BMFF and age, BMI or adiposity traits.**

427 In addition to BMD, factors including age, BMI and peripheral adiposity have been
428 associated with altered BMFF. Thus, an important question is whether such other
429 factors confound the relationships between BMFF and BMD. To address this, we first
430 used univariable linear regression to identify other variables significantly associated
431 with BMFF at each site, thereby identifying factors associated with BMFF and/or BMD.
432 The results are presented in Supplemental Table 5.
433

434 We found that spinal BMFF was positively associated with age, VAT mass, total fat %,
435 android fat %, gynoid fat % and trunk fat % in males and females, with no sex

436 differences in these relationships. In contrast, spinal BMFF showed a positive
437 association with legs fat % in males only (Supplemental Table 5).

438
439 Fewer variables were associated with BMFF at the femoral head or total hip. The
440 former showed a positive relationship only with age, and in females only, while the
441 latter was negatively associated only with BMI across both sexes. However, no other
442 variables were associated with BMFF at these two sites (Supplemental Table 5). In
443 contrast, diaphyseal BMFF was associated with several of the variables assessed,
444 often in a sexually dimorphic manner. Thus, across both sexes, diaphyseal BMFF was
445 inversely associated with VAT mass, while inverse associations with total fat %,
446 android fat % and trunk fat % showed significant sex differences, occurring in females
447 but not in males. In contrast, in males, but not females, diaphyseal BMFF was
448 positively associated with legs fat % (Supplemental Table 5).

449 450 **3.6. The inverse association between BMFF and BMD at each site persists after** 451 **controlling for relevant covariables.**

452 Based on the univariable associations identified in Supplemental Tables 1-5, we next
453 constructed multivariable models to estimate the true relationship between BMFF and
454 BMD at each site. Table 4 shows the results for BMD spine as the dependent variable.
455 Here, the best predictive model was obtained when including BMFF Spine, sex, BMI,
456 Legs fat %, VAT mass and Android fat % as covariables (Model 4.6). Notably, the
457 inverse association between spinal BMFF and spinal BMD persisted even when
458 accounting for these other covariables. Moreover, inclusion of leg fat, VAT mass and
459 android fat weakened the size of the sex effect, suggesting that increased spinal BMD
460 in males is explained, at least in part, by their lower amount of leg fat and greater VAT
461 mass and android fat.

462
463 Table 5 shows the results for femoral neck BMD as the dependent variable. Here,
464 separate models were tested for BMFF at the femoral head, total hip or spine as the
465 main explanatory variables; the former was assessed in females only because of the
466 lack of relationship between femoral head BMFF and femoral neck BMD in males
467 (Supplemental Table 2). We found that, in females, the significant inverse association
468 between BMFF femoral head and femoral neck BMD persisted when accounting for
469 BMI and legs fat % (Model 5.3). Similarly, across both sexes, total hip or spine BMFF
470 retained their inverse relationships with femoral neck BMD even after accounting for
471 sex, BMI and legs fat % (Models 5.6 and 5.11). The best model for BMFF total hip also
472 included Android fat % and Trunk fat % (Model 5.8). Notably, male sex was no longer
473 associated with increased femoral neck BMD when controlling for BMFF spine, BMI
474 and legs fat % (Model 5.11), suggesting that males have greater BMD at the femoral
475 neck because they tend to have lower spinal BMFF, lower % leg fat and higher BMI
476 than females.

477
478 Given that spine BMFF is positively associated with total hip BMFF (Table 3), we
479 postulated that the inverse relationship between spine BMFF and femoral neck BMD
480 may occur because spine BMFF is a surrogate for total hip BMFF. However, the
481 inverse relationship between spine BMFF and femoral neck BMD persisted even when
482 accounting for BMFF at the total hip (Model 5.12), demonstrating that these
483 explanatory variables are acting at least partly independently of each other.

484

485 Multivariable regression for total hip BMD is presented in Table 6. The best predictive
486 model included BMFF total hip, sex, BMI and legs fat % as the covariables (Model
487 6.3); inclusion of VAT mass (Model 6.4) did not further improve the model, despite
488 VAT mass showing a significant univariable association with total hip BMD
489 (Supplemental Table 3). Notably, the inverse relationship between total hip BMD and
490 BMFF persisted even when accounting for sex, BMI and legs fat %, confirming total
491 hip BMFF as an independent predictor of BMD at this site.

492

493 Finally, Table 7 shows the results of multivariable regression for femoral shaft BMD.
494 Here, the best predictive model included diaphyseal BMFF, sex, BMI, legs fat % and
495 android fat % (Model 7.5), although a similarly accurate model was obtained when
496 VAT mass and trunk fat % were also included (Model 7.7). As for the other BMFF-
497 BMD relationships, BMFF at the diaphysis retained its significant inverse association
498 with femoral shaft BMD even when these other covariables were accounted for.
499 Moreover, males no longer had significant increases in femoral shaft BMD when
500 controlling for BMFF diaphysis, BMI and legs fat % (Model 7.3-7.7). This suggests that
501 males may have greater femoral shaft BMD because they have a higher BMI and lower
502 % leg fat than females.

503 4. DISCUSSION

504 Herein, we have developed a new deep learning method for analysis of BM adiposity
505 using Dixon MRI data from the UKBB. This is the first study to establish deep learning
506 for BM segmentation at multiple sites, and the first do so, for any skeletal site, in the
507 UKBB imaging study. Our models yield BMFF measurements that are consistent with
508 previous observations, including sex differences in spinal BMFF and inverse
509 associations with BMD. This demonstrates the ability of our models to generate
510 accurate, reliable BMFF measurements from the UKBB MRI data. We further reveal
511 new site- and sex-specific associations that have not been reported previously,
512 highlighting the potential of our methods to uncover new pathophysiological functions
513 of BMAT.

514

515 4.1. Deep learning for large-scale BM analysis

516 Several other recent studies have developed deep learning for automated BM
517 segmentation from MRI data. For example, von Brandis *et al* assessed the feasibility
518 of deep learning for segmenting BM from T2-weighted Dixon water-only images,
519 focusing on the knee region (20); however, the best median dice score of their model
520 was only 0.68, far below that obtained by our models (Table 2). Better accuracy was
521 achieved by Zhou *et al*, who established a deep learning model for segmenting lumbar
522 vertebrae from Dixon MRI data (18). They trained their model using manual
523 segmentations of 165 vertebrae from 31 subjects, with the model then tested on a
524 validation set of 24 subjects. They achieved an average dice score of 0.849, below the
525 accuracy of our vertebral ROI-Attention-U-Net (Table 2). More recently, Zhao *et al*
526 used deep learning for segmenting lumbar vertebrae from modified Dixon MRI data,
527 using a training set of 142 subjects and a validation set of 64 subjects (19). Their model
528 achieved a mean dice score of 0.912, the same as that obtained by our vertebral ROI-
529 Attention-U-Net (Table 2). Thus, among deep learning models for segmenting
530 vertebral BM, our model achieves an accuracy that is similar or greater than that
531 obtained by others.

532

533 Notably, our study is the first to develop deep learning for BM segmentation at the
534 femoral head, total hip and femoral diaphysis. This is important because the properties
535 of BMAT vary according to skeletal location (1, 7, 8). Thus, to fully understand the
536 health implications of BMAT and its potential utility as a clinical biomarker, it is critical
537 to assess BMFF at other sites. Indeed, as discussed below, we found that the
538 associations between BMFF, age, BMD, BMI and peripheral adiposity differ according
539 to the BM region assessed, underscoring the importance of assessing BMFF across
540 multiple sites. Finally, our model includes dedicated error-checking steps to remove
541 inaccurate segmentation outputs, which is essential for reliable analysis of large-scale
542 MRI data.

543

544 4.2. New ROI attention U-Net model

545 Another advance of the present study is our development of a new ROI attention U-
546 Net model that allows accurate segmentation of small VOIs from large volumetric data.
547 The traditional 3D U-Net has a fixed receptive field that is dependent on the size of
548 convolutional kernels and network depth. To achieve state-of-the-art performance, the
549 network architecture needs to be carefully designed to fit the sizes of the segmented
550 objects and image resolution. As a result, in this study the traditional 3D U-Net
551 generates highly accurate results for vertebrae and femoral head (Table 2), regions in
552 which the segmented objects are relatively large. However, this traditional U-Net

553 shows limited discriminative power when dealing with smaller structures such as the
554 femoral diaphysis, where only a few pixels on each axial slice are annotated as
555 foreground. On the contrary, our new ROI attention U-Net model can adaptively
556 encode the local and global contextual information with its adjustive-attention
557 mechanism. As shown in Table 2, it increased segmentation accuracy of the femoral
558 diaphysis by over 25% and also slightly improved accuracy for the total hip region.
559 Alongside these improvements, for the femoral head and vertebrae the ROI attention
560 U-Net performs similarly to the carefully designed traditional 3D U-Net (Table 2). Thus,
561 our new ROI attention model advances the state of the art by achieving accurate
562 segmentation of both larger and smaller objects.

563 564 **4.3. Association between BMFF and pathophysiological characteristics –** 565 **confirmation of previous studies and new findings**

566 The key aim of our study was to develop and validate deep learning models for
567 automated BM segmentation of UKBB Dixon MRI data. Our group of 729 subjects is
568 the largest cohort yet to undergo measurement of spinal BMFF, and by far the largest
569 to include assessment of BMFF at any femoral site (12). Consistent with previous
570 reports, we find that spinal BMFF is lower than femoral BMFF (Fig. 4) (1, 12, 31); is
571 greater in females than in males (Fig. 4) (29, 30); increases with age (Supplemental
572 Table 5) (12, 29, 30, 32); is elevated in osteopaenia or osteoporosis, at least in females
573 (Fig. 5) (1, 6, 12); exhibits a robust, inverse association with spinal BMD (Table 4) (1,
574 6, 12); and is positively associated with visceral adiposity (Supplemental Table 5) (32,
575 33).

576
577 Our results for femoral BMFF are also consistent with previous studies. For example,
578 in a cohort of aged females, Griffith *et al* found that BMFF in the femoral head, neck
579 and diaphysis is increased in osteoporosis and inversely associated with BMD at each
580 site (34). We confirm these findings (Fig. 5, Tables 5-7) and further reveal that femoral
581 head BMFF is not associated with BMD at the femoral neck or total hip in males
582 (Supplemental Tables 2-3). We also show that diaphyseal BMFF is typically inversely
583 associated with peripheral adiposity in females but not in males, while BMFF at the
584 femoral head or total hip is not associated with these peripheral adiposity traits
585 (Supplemental Table 5); these observations confirm and extend those of a previous
586 smaller-scale study (35). The reasons for these variable site- and sex-dependent
587 relationships between BMFF and peripheral adiposity remain to be determined;
588 however, one possibility is that they reflect preferences for the partitioning of lipid
589 storage between different adipose depots.

590
591 Many of our new findings relate to the fact that most previous MR-based studies of
592 BM adiposity have focussed on vertebrae, with femoral sites being relatively
593 overlooked (12). For example, we show that, across both sexes, BMFF is highest in
594 the femoral head and decreases progressively in the total hip and diaphysis, while
595 BMFF at each femoral site is greater in males than in females (Fig. 4). Unlike in the
596 spine, age is associated with increased femoral head BMFF only in females, and
597 across both sexes shows no relationship with total hip or diaphyseal BMFF
598 (Supplemental Table 5). This could reflect the fact that, compared to the spine, these
599 femoral sites contain a greater proportion of constitutive BMAT, which is less age
600 responsive than the regulated BMAT that predominates in the axial skeleton (7, 8).
601 However, it may be that age-related increases in femoral BMAT occur over a longer

602 timeframe that would only be apparent when BMFF is assessed over a greater age
603 range.

604

605 Regarding constitutive vs regulated subtypes, we also find robust positive associations
606 between BMFF at the four different sites analysed (Table 3), similar to the findings of
607 Slade *et al* (31). However, we further reveal that these relationships exhibit sex
608 differences and are strongest between the three femoral regions, with spinal BMFF
609 showing no association with diaphyseal BMFF (Table 3). This may reflect differences
610 in the development and function of regulated vs constitutive BMAT (7, 8).

611

612 Together, our present findings confirm those of previous studies while also revealing
613 new knowledge about BMAT's site- and sex-dependent characteristics. This
614 underscores the ability of our deep learning models to yield reliable BMFF
615 measurements and to identify new insights into the pathophysiology of BMAT.

616

617 **4.4. Limitations**

618 One specific limitation is that our cohort included relatively few osteoporotic males.
619 This restricted our ability, in males, to detect significant effects of osteoporosis on
620 BMFF at each site. Our univariable and multivariable regression analyses were still
621 able to detect significant inverse associations between BMFF and BMD at each site;
622 however, once we have measured BMFF across the full available UKBB cohort it will
623 be informative to reassess the relationship between BMFF and osteoporosis.

624

625 A more-general limitation relates to the UKBB MRI protocol. Participants in the UKBB
626 imaging study visited several different imaging centres for acquisition of the MRI
627 scans. Therefore, across these different imaging centres the MRI protocol parameters
628 had to be standardised and harmonised, resulting in both advantages and drawbacks.
629 For example, to simplify the procedure the Dixon sequences were based on only two
630 echo times; however, with only dual-echo sequences, no accurate T2*-correction
631 could be applied and the complexity of the fat spectrum could not be considered in the
632 BMFF mapping (10, 14). As a result, reported BMFF measurements can be affected
633 by T2* decay effects caused by the presence of trabecular bone, which in turn may
634 differ in the water and fat components (9, 10). However, the moderately low flip angle
635 (10°) is acceptable to limit T1-bias, and protocol standardisation compelled all
636 examinations to be performed in similar conditions, with the exact same parameters
637 (9, 36). Consequently, even if the true proton-density fat fraction (PDFF) could not be
638 quantified, a comparable estimate could be obtained through the reported BMFF,
639 which permits group comparison and method cross-validation. Furthermore, dual-
640 echo Dixon-derived BMFF allows the derivation of consistent 3D BMFF measurements
641 across all UKBB MR imaging centres. This is very important for our BMFF validation
642 study, as it allowed us to assess and automate extraction of BMFF maps from multiple
643 skeletal sites, on a 3D mode.

644

645 **4.5. Conclusions**

646 Our new deep learning models allow accurate segmentation of small VOIs from large
647 volumetric MRI data. While we have used these models to analyse small BM regions,
648 they could also be applied for precise, automated, large-scale analysis of other small
649 anatomical structures of interest. The development and validation of our models using
650 UKBB MRI data is hugely significant because, unlike most other MRI datasets, the
651 UKBB also provides extensive genetic and phenotypic data for each subject, including

652 whole-genome sequencing and health records. This linked data allows comprehensive
653 association studies to identify the genetic and pathophysiological factors associated
654 with FF and other MRI-derived measurements. Indeed, Liu *et al*/ recently demonstrated
655 the power of this approach using deep learning for segmentation of abdominal organs
656 from UKBB MRI data (16). They identified genetic variants and clinical conditions
657 associated with FF and other imaging-derived characteristics for each organ, as well
658 as combinations of characteristics across multiple organs. The deep learning models
659 established in the present study unlock similar possibilities: using these new models,
660 we will next measure BMFF across the full UKBB imaging cohort, which will eventually
661 include 100,000 subjects. This will allow us to identify the genetic, physiological and
662 clinical conditions associated with altered BMFF at each site. Such knowledge will help
663 to elucidate the mechanisms that influence BM adiposity and reveal, to an
664 unprecedented extent, how BMAT impacts human health and disease.

665 **ACKNOWLEDGEMENTS**

666

667 This work was supported by a grant from the Medical Research Council
668 (MR/S010505/1 to W.P.C.). W.P.C. was further supported by a Chancellor's
669 Fellowship from the University of Edinburgh. C.W. was further supported by the British
670 Heart Foundation (RG/16/10/32375). C.G. and T.M. were supported by the Edinburgh
671 Clinical Research Facility and NHS Lothian R&D.

672

673 We are grateful to Dominic Job (Edinburgh Imaging, University of Edinburgh) for
674 support with IT infrastructure, and Jimmy Bell, Louise Thomas and Brandon Witcher
675 (University of Westminster) for helpful discussions and advice regarding working with
676 UKBB MRI data.

677 **AUTHOR CONTRIBUTIONS** (based on [CRediT taxonomy](#))

678

679 **Conceptualisation**, W.P.C.; **Data curation**, D.M.M., C.W., G.P. and W.P.C.; **Formal**
680 **Analysis**, D.M.M., C.W., G.P., C.D.G. and W.P.C.; **Funding Acquisition**, , S.I.K.S.,
681 T.M. and W.P.C.; **Investigation**, D.M.M., C.W., G.P. and W.P.C.; **Methodology**,
682 D.M.M., C.W., G.P., C.D.G., S.B., J.P., S.I.K.S., T.M. and W.P.C.; **Project**
683 **administration**, S.I.K.S., T.M. and W.P.C.; **Resources**, S.I.K.S., T.M. and W.P.C.;
684 **Software**, D.M.M., C.W., G.P.; **Supervision**, S.I.K.S., T.M. and W.P.C.;
685 **Visualisation**, D.M.M., C.W., C.D.G. and W.P.C.; **Writing – Original Draft**, D.M.M.,
686 C.W., S.B., J.P. and W.P.C.; **Writing – Review & Editing**, D.M.M., C.W., G.P.,
687 C.D.G., S.B., J.P., S.I.K.S., T.M. and W.P.C.

688 **REFERENCES**

- 689 1. Cawthorn WP. Bone Marrow Adipose Tissue. In: Zaidi M, ed. Encyclopedia of
690 Bone Biology. Oxford, UK: Oxford: Academic Press; 2020:156-77.
- 691 2. Devlin MJ, Cloutier AM, Thomas NA, et al. Caloric restriction leads to high marrow
692 adiposity and low bone mass in growing mice. *J Bone Miner Res.*
693 2010;25(9):2078-88.
- 694 3. Cawthorn WP, Scheller EL, Learman BS, et al. Bone Marrow Adipose Tissue Is
695 an Endocrine Organ that Contributes to Increased Circulating Adiponectin during
696 Caloric Restriction. *Cell Metabolism.* 2014;20(2):368-75.
- 697 4. Cawthorn WP, Scheller EL, Parlee SD, et al. Expansion of Bone Marrow Adipose
698 Tissue During Caloric Restriction Is Associated With Increased Circulating
699 Glucocorticoids and Not With Hypoleptinemia. *Endocrinology.* 2016;157(2):508-
700 21.
- 701 5. Suchacki KJ, Tavares AAS, Mattiucci D, et al. Bone marrow adipose tissue is a
702 unique adipose subtype with distinct roles in glucose homeostasis. *Nature*
703 *Communications.* 2020;11(1):3097.
- 704 6. Veldhuis-Vlug AG, Rosen CJ. Clinical implications of bone marrow adiposity. *J*
705 *Intern Med.* 2018;283(2):121-39.
- 706 7. Craft CS, Li Z, MacDougald OA, Scheller EL. Molecular differences between
707 subtypes of bone marrow adipocytes. *Current Molecular Biology Reports.*
708 2018;4(1):16-23.
- 709 8. Scheller EL, Doucette CR, Learman BS, et al. Region-specific variation in the
710 properties of skeletal adipocytes reveals regulated and constitutive marrow
711 adipose tissues. *Nat Commun.* 2015;6:7808.
- 712 9. Tratwal J, Labella R, Bravenboer N, et al. Reporting Guidelines, Review of
713 Methodological Standards, and Challenges Toward Harmonization in Bone
714 Marrow Adiposity Research. Report of the Methodologies Working Group of the
715 International Bone Marrow Adiposity Society. *Frontiers in Endocrinology.*
716 2020;11(65).
- 717 10. Karampinos DC, Ruschke S, Dieckmeyer M, et al. Quantitative MRI and
718 spectroscopy of bone marrow. *J Magn Reson Imaging.* 2018;47(2):332-53.
- 719 11. Cordes C, Baum T, Dieckmeyer M, et al. MR-Based Assessment of Bone Marrow
720 Fat in Osteoporosis, Diabetes, and Obesity. *Front Endocrinol (Lausanne).*
721 2016;7:74.
- 722 12. Sollmann N, Löffler MT, Kronthaler S, et al. MRI-Based Quantitative Osteoporosis
723 Imaging at the Spine and Femur. *Journal of Magnetic Resonance Imaging.*
724 2021;54(1):12-35.
- 725 13. Shen W, Chen J, Gantz M, et al. MRI-measured pelvic bone marrow adipose
726 tissue is inversely related to DXA-measured bone mineral in younger and older
727 adults. *European journal of clinical nutrition.* 2012;66(9):983-8.
- 728 14. Littlejohns TJ, Holliday J, Gibson LM, et al. The UK Biobank imaging enhancement
729 of 100,000 participants: rationale, data collection, management and future
730 directions. *Nature Communications.* 2020;11(1):2624.
- 731 15. Kart T, Fischer M, Küstner T, et al. Deep Learning-Based Automated Abdominal
732 Organ Segmentation in the UK Biobank and German National Cohort Magnetic
733 Resonance Imaging Studies. *Invest Radiol.* 2021;56(6):401-8.
- 734 16. Liu Y, Bastý N, Whitcher B, et al. Genetic architecture of 11 organ traits derived
735 from abdominal MRI using deep learning. *eLife.* 2021;10:e65554.

- 736 17. Suinesiaputra A, Sanghvi MM, Aung N, et al. Fully-automated left ventricular mass
737 and volume MRI analysis in the UK Biobank population cohort: evaluation of initial
738 results. *Int J Cardiovasc Imaging*. 2018;34(2):281-91.
- 739 18. Zhou J, Damasceno PF, Chachad R, et al. Automatic Vertebral Body
740 Segmentation Based on Deep Learning of Dixon Images for Bone Marrow Fat
741 Fraction Quantification. *Frontiers in Endocrinology*. 2020;11(612).
- 742 19. Zhao Y, Zhao T, Chen S, et al. Fully automated radiomic screening pipeline for
743 osteoporosis and abnormal bone density with a deep learning-based
744 segmentation using a short lumbar mDixon sequence. *Quantitative Imaging in
745 Medicine and Surgery*. 2022;12(2):1198-213.
- 746 20. von Brandis E, Jenssen HB, Avenarius DFM, et al. Automated segmentation of
747 magnetic resonance bone marrow signal: a feasibility study. *Pediatric Radiology*.
748 2022;52(6):1104-14.
- 749 21. Gondim Teixeira PA, Cherubin T, Badr S, et al. Proximal femur fat fraction
750 variation in healthy subjects using chemical shift-encoding based MRI. *Sci Rep*.
751 2019;9(1):20212.
- 752 22. Çiçek Ö, Abdulkadir A, Lienkamp SS, et al. 3D U-Net: Learning Dense Volumetric
753 Segmentation from Sparse Annotation. 2016. Cham. Springer International
754 Publishing: 424-32.
- 755 23. Ronneberger O, Fischer P, Brox T. U-Net: Convolutional Networks for Biomedical
756 Image Segmentation. 2015. Cham. Springer International Publishing: 234-41.
- 757 24. Woo S, Park J, Lee J-Y, Kweon IS. CBAM: Convolutional Block Attention Module.
758 2018. Cham. Springer International Publishing: 3-19.
- 759 25. Wang X, Girshick RB, Gupta A, He K. Non-local Neural Networks. 2018 IEEE/CVF
760 Conference on Computer Vision and Pattern Recognition. 2018:7794-803.
- 761 26. Paszke A, Gross S, Chintala S, et al. Automatic differentiation in PyTorch. 2017.
- 762 27. Kingma DP, Ba J. Adam: A Method for Stochastic Optimization. *CoRR*.
763 2015;abs/1412.6980.
- 764 28. finalfit: Quickly Create Elegant Regression Results Tables and Plots when
765 Modelling [computer program]. Version R package version 1.0.5; 2022.
- 766 29. Griffith JF, Yeung DK, Ma HT, et al. Bone marrow fat content in the elderly: a
767 reversal of sex difference seen in younger subjects. *J Magn Reson Imaging*.
768 2012;36(1):225-30.
- 769 30. Baum T, Rohrmeier A, Syväri J, et al. Anatomical Variation of Age-Related
770 Changes in Vertebral Bone Marrow Composition Using Chemical Shift Encoding-
771 Based Water–Fat Magnetic Resonance Imaging. *Frontiers in Endocrinology*.
772 2018;9:141.
- 773 31. Slade JM, Coe LM, Meyer RA, McCabe LR. Human bone marrow adiposity is
774 linked with serum lipid levels not T1-diabetes. *Journal of diabetes and its
775 complications*. 2012;26(1):1-9.
- 776 32. Hasic D, Lorbeer R, Bertheau RC, et al. Vertebral Bone Marrow Fat Is
777 independently Associated to VAT but Not to SAT: KORA FF4—Whole-Body MR
778 Imaging in a Population-Based Cohort. *Nutrients*. 2020;12(5):1527.
- 779 33. Bredella MA, Torriani M, Ghomi RH, et al. Vertebral Bone Marrow Fat Is Positively
780 Associated With Visceral Fat and Inversely Associated With IGF-1 in Obese
781 Women. *Obesity (Silver Spring)*. 2011.
- 782 34. Griffith JF, Yeung DK, Tsang PH, et al. Compromised bone marrow perfusion in
783 osteoporosis. *J Bone Miner Res*. 2008;23(7):1068-75.
- 784 35. Bredella MA, Fazeli PK, Miller KK, et al. Increased bone marrow fat in anorexia
785 nervosa. *J Clin Endocrinol Metab*. 2009;94(6):2129-36.

- 786 36. Liu CY, McKenzie CA, Yu H, et al. Fat quantification with IDEAL gradient echo
787 imaging: correction of bias from T(1) and noise. Magn Reson Med.
788 2007;58(2):354-64.

789 **TABLES**
790

	Males (n = 277)			F (n = 452)		
	Control (n=138)	Osteopaenic (n=146)	Osteoporotic (n=17)	Control (n=134)	Osteopaenic (n=262)	Osteoporotic (n=70)
Age (years)	65 [63, 67]	65 [63, 67]	64.47 ± 0.7	65 [62, 67]	65 [62, 67]	65 [63, 67]
BMI (kg/m ²)	23.6 [22.8, 24.3]	23.3 [22.3, 24.1]	22.04 ± 0.20 ***	22.9 [21.7, 23.9] ##	22.6 [21.3, 23.7]	21.67 ± 0.40 *
BMD T-score (L1-L4)	0.65 [-0.2, 1.775]	-1 [-1.575, -0.1] ***	-3 [-3.25, -1.55] ***	0.15 [-0.4, 0.9]	-1.5 [-1.9, -0.8] ***	-2.8 [-3.1, -2.6] ***
BMD T-score (total femur, left)	0.2 [-0.3, 0.7]	-1.12 ± 0.05 ***	-2.2 ± 0.14 ***	0 [-0.4, 0.475]	-1.4 [-1.8, -1] ***	-2.22 ± 0.09 ***
BMD T-score (femoral neck, left)	-0.3 [-0.7, 0.275]	-1.5 [-1.8, -1.2] ***	-2.45 ± 0.13 ***	-0.15 [-0.7, 0.4]	-1.45 [-1.8, -1.1] ***	-2.11 ± 0.07 ***
Android tissue fat % by DXA	30.6 [24, 34.6]	30.0 [22.8, 35.7]	24.4 ± 2.0	34.8 [27.8, 40.7] ###	32.5 ± 0.6	31.0 ± 1.1
Gynoid tissue fat % by DXA	24.3 ± 0.4	24.4 ± 0.4	23.5 ± 1.0	37.6 ± 0.4 ###	38.5 ± 0.3	38.7 ± 0.6
Legs tissue fat % by DXA	20.9 ± 0.3	21.2 ± 0.3	21.3 ± 1.0	35.2 ± 0.5 ###	36.9 ± 0.3	37.1 ± 0.6
Trunk tissue fat % by DXA	29.1 [23.7, 32.0]	28.6 [23.0, 33.4]	24.3 ± 1.5	35.4 [29.9, 39.5] ###	33.3 ± 0.4	32.3 ± 0.9
Total tissue fat % by DXA	24.6 ± 0.4	25.6 [21.6, 28.5]	22.9 ± 1.8	34.7 [30.9, 37.38] ###	34.3 ± 0.3	33.9 ± 0.6
VAT mass (g)	949.4 ± 35.25	783.5 [465.5, 1131]	586 ± 79.6 **	407 [225.5, 717] ###	346.5 [217, 563.5]	296 [193.3, 526.5]

791
792 **Table 1 – Characteristics of subjects in training and validation cohort.** Normally
793 distributed data are reported as mean ± SEM while non-normally distributed data are
794 reported as median [interquartile range]. BMI, body mass index; DXA, dual-energy X-
795 ray absorptiometry; VAT, visceral adipose tissue. Within each sex, significant
796 differences between control subjects and osteopaenic or osteoporotic subjects are
797 indicated by * (*P* <0.05), ** (*P* <0.01) or *** (*P* <0.001). Within control subjects,
798 significant differences between males and females are indicated by ## (*P* <0.01) or ###
799 (*P* <0.001).

	Vertebrae	Femoral head	Total Hip	Femoral Diaphysis
U-Net	0.925	0.951	0.904	0.69
ROI-Attention-U-Net	0.912	0.945	0.912	0.866

800

801

802

Table 2 – Segmentation Accuracy (dice scores) of the traditional U-Net and our CBAM-ROI-attention U-Net.

Explanatory	Dependent	Sex	β (CIs)	Adj. R ²	P (Exp)	P (Exp*Sex)
BMFF Spine	BMFF Femoral Head	Both	0.037 (0.015, 0.059)	0.015	1.25E-03	2.6E-04
		Female	0.109 (0.08, 0.138)	0.118	8.69E-13	-
		Male	0.028 (0, 0.057)	0.013	0.049	-
	BMFF Total Hip	Both	0.091 (0.063, 0.12)	0.055	4.48E-10	0.026
		Female	0.171 (0.132, 0.21)	0.145	2.16E-16	-
	Male	0.106 (0.069, 0.144)	0.107	7.22E-08	-	
BMFF Diaphysis	Both	0.054 (0.01, 0.099)	0.007	0.017	0.801	
BMFF Femoral Head	BMFF Total Hip	Both	1.011 (0.939, 1.082)	0.552	1.18E-111	0.474
	BMFF Diaphysis	Both	0.818 (0.674, 0.962)	0.169	1.69E-26	0.534
BMFF Total Hip	BMFF Diaphysis	Both	0.764 (0.669, 0.858)	0.281	2.48E-48	0.001
		Female	0.65 (0.534, 0.766)	0.228	8.76E-25	-
		Male	1.046 (0.857, 1.234)	0.331	1.03E-22	-

803 **Table 3 – Univariable and sex-stratified associations between BMFF for each**
804 **region.** To test if the explanatory-dependent relationship differs between males and
805 F, a linear model was first analysed across both sexes, with sex included as an
806 interacting variable. Beta coefficients are shown (with lower and upper 95% CIs in
807 brackets), followed by the adjusted R² (Adj. R²) and unadjusted P value for each
808 explanatory variable (P Exp). P values were also calculated for the Explanatory*Sex
809 interaction (P Exp*Sex); if significant, additional linear models were analysed in
810 females and males separately. Because 12 correlations were assessed, the
811 Bonferroni-adjusted alpha level for P (Exp) is 0.05/12 = 0.0042. Significant
812 explanatory-dependent relationships are highlighted in bold.

	<i>Covariable</i>							
	Adj. R ²	AIC	BMFF Spine	Sex (M)	BMI	Legs fat %	VAT mass (kg)	Android fat %
Model 4.1	0.39	-893.1	-0.004 (-0.006 to -0.003)***	0.177 (0.156 to 0.198)***	-	-	-	-
Model 4.2	0.43	-941.9	-0.005 (-0.006, -0.003)***	0.158 (0.137, 0.179)***	0.023 (0.017, 0.030)***	-	-	-
Model 4.3	0.46	-975.3	-0.004 (-0.006, -0.003)***	0.061 (0.023, 0.098)**	0.029 (0.023, 0.036)***	-0.006 (-0.008, -0.004)***	-	-
Model 4.4	0.47	-990.7	-0.005 (-0.006, -0.004)***	0.037 (-0.002, 0.075)	0.022 (0.015, 0.029)***	-0.006 (-0.008, -0.004)***	0.064 (0.033, 0.095)***	-
Model 4.5	0.47	-990.1	-0.005 (-0.006, -0.004)***	0.058 (0.020, 0.095)**	0.021 (0.014, 0.029)***	-0.007 (-0.009, -0.005)***	-	0.003 (0.001, 0.004)***
Model 4.6	0.47	-990.9	-0.005 (-0.007, -0.004)***	0.043 (0.004, 0.083)*	0.021 (0.013, 0.028)***	-0.007 (-0.009, -0.004)***	0.041 (-0.003, 0.085)	0.001 (-0.000, 0.003)

813 **Table 4 – Multivariable regression analyses for spine BMD.** Multivariable
814 regression was done using BMD spine as the dependent variable; explanatory
815 variables were selected based on those showing significant univariable association
816 with BMD spine and/or BMFF at the relevant sites, as shown in Supplemental Tables
817 1-5. For each model the adjusted R² (Adj. R²) and Akaike Information Criterion (AIC)
818 are shown, along with multivariable beta coefficients (with lower and upper 95% CIs)
819 for each variable. *P* values are indicated by * (*P*<0.05), ** (*P*<0.01) or *** (*P*<0.001),
820 with significant associations highlighted in bold

	Covariable									
	Adj. R²	AIC	BMFF Femoral Head	BMFF Total Hip	BMFF Spine	Sex (M)	BMI	Legs fat %	Android fat %	Trunk fat %
Model 5.1	0.11	-658.8	-0.011 (-0.015, -0.008)***	-	-	-	-	-	-	-
Model 5.2	0.12	-662.2	-0.011 (-0.014, -0.008)***	-	-	-	0.008 (0.001, 0.015)*	-	-	-
Model 5.3	0.13	-669.9	-0.011 (-0.014, -0.007)***	-	-	-	0.012 (0.005, 0.019)**	-0.003 (-0.006, -0.001)**	-	-
Model 5.4	0.24	-1083.6	-	-0.015 (-0.018, -0.012)***	-	0.122 (0.104, 0.140)***	-	-	-	-
Model 5.5	0.25	-1093.3	-	-0.014 (-0.017, -0.011)***	-	0.114 (0.096, 0.132)***	0.010 (0.004, 0.016)**	-	-	-
Model 5.6	0.27	-1104.8	-	-0.013 (-0.016, -0.010)***	-	0.057 (0.022, 0.092)**	0.014 (0.008, 0.020)**	-0.003 (-0.005, -0.002)***	-	-
Model 5.7	0.28	-1107.1	-	-0.013 (-0.016, -0.010)***	-	0.057 (0.022, 0.092)**	0.017 (0.010, 0.024)***	-0.003 (-0.005, -0.001)**	-0.001 (-0.002, -0.000)*	-
Model 5.8	0.27	-1108.1	-	-0.013 (-0.016, -0.010)***	-	0.066 (0.030, 0.102)***	0.017 (0.010, 0.024)***	-0.004 (-0.006, -0.002)***	-0.007 (-0.014, -0.000)*	0.008 (-0.001, 0.017)
Model 5.9	0.20	-1039.1	-	-	-0.004 (-0.006, -0.003)***	0.077 (0.059, 0.096)***	-	-	-	-
Model 5.10	0.22	-1058.1	-	-	-0.005 (-0.006, -0.003)***	0.066 (0.047, 0.085)***	0.014 (0.008, 0.019)***	-	-	-
Model 5.11	0.24	-1071.5	-	-	-0.004 (-0.006, -0.003)***	0.007 (-0.028, 0.042)	0.017 (0.011, 0.023)***	-0.004 (-0.006, -0.002)***	-	-
Model 5.12	0.29	-1089.6	-	-0.011 (-0.014, -0.008)***	-0.003 (-0.004, -0.001)***	0.053 (0.016, 0.090)**	0.015 (0.008, 0.022)***	-0.004 (-0.006, -0.002)***	-0.007 (-0.014, -0.001)*	0.009 (0.000, 0.018)*

822 **Table 5 – Multivariable regression analyses for femoral neck BMD.** Multivariable regression was done using femoral neck BMD
823 as the dependent variable, with BMFF at the femoral head, total hip and spine chosen as the primary explanatory variables. Other
824 explanatory covariables were selected, models constructed, and data presented as described for Table 4. Models with femoral head
825 BMFF (5.1, 5.2 and 5.3) were tested in females only because univariable analysis showed that this is not associated total hip BMD
826 in males (Supplemental Table 2).

827

	<i>Covariable</i>						
	Adj. R ²	AIC	BMFF Total Hip	Sex (M)	BMI	Legs fat %	VAT mass (kg)
Model 6.1	0.34	-997.9	-0.017 (-0.020, -0.014)***	0.170 (0.152, 0.189)***	-	-	-
Model 6.2	0.37	-1029.2	-0.016 (-0.019, -0.013)***	0.156 (0.137, 0.175)***	0.018 (0.012, 0.023)***	-	-
Model 6.3	0.39	-1056.6	-0.015 (-0.018, -0.012)***	0.069 (0.033, 0.105)***	0.023 (0.017, 0.029)***	-0.005 (-0.007, -0.003)***	-
Model 6.4	0.39	-1051.3	-0.015 (-0.018, -0.012)***	0.074 (0.037, 0.111)***	0.025 (0.018, 0.032)***	-0.005 (-0.007, -0.003)***	-0.016 (-0.045, 0.012)

828

829

830

831

832

833

Table 6 – Multivariable regression analyses for total hip BMD. Multivariable regression was done using total hip BMD as the dependent variable, with BMFF at the total hip as the primary explanatory variable. Other explanatory covariables were selected, models constructed, and data presented as described for Table 4.

	<i>Covariable</i>								
	Adj. R ²	AIC	BMFF Diaphysis	Sex (M)	BMI	Legs fat %	VAT mass (kg)	Android fat %	Trunk fat %
Model 7.1	0.28	-693.2	-0.014 (-0.016, -0.011)***	0.164 (0.141, 0.187)***	-	-	-	-	-
Model 7.2	0.30	-711.7	-0.013 (-0.016, -0.011)***	0.151 (0.127, 0.174)***	0.017 (0.010, 0.025)***	-	-	-	-
Model 7.3	0.33	-743.1	-0.013 (-0.016, -0.011)***	0.035 (-0.010, 0.080)	0.025 (0.017, 0.032)***	-0.007 (-0.010, -0.005)***	-	-	-
Model 7.4	0.33	-739.5	-0.013 (-0.016, -0.011)***	0.045 (-0.002, 0.091)	0.028 (0.019, 0.037)***	-0.007 (-0.010, -0.005)***	-0.029 (-0.065, 0.007)	-	-
Model 7.5	0.34	-747.1	-0.014 (-0.016, -0.011)***	0.038 (-0.007, 0.083)	0.030 (0.021, 0.039)***	-0.006 (-0.009, -0.004)***	-	-0.002 (-0.004, -0.000)*	-
Model 7.6	0.34	-745.3	-0.013 (-0.016, -0.011)***	0.035 (-0.010, 0.080)	0.030 (0.021, 0.039)***	-0.006 (-0.009, -0.004)***	-	-	-0.002 (-0.004, -0.000)*
Model 7.7	0.34	-743.4	-0.014 (-0.016, -0.011)***	0.047 (-0.002, 0.096)	0.030 (0.020, 0.039)***	-0.008 (-0.011, -0.005)***	0.007 (-0.044, 0.059)	-0.011 (-0.020, -0.002)*	0.012 (0.000, 0.024)*

834 **Table 7 – Multivariable regression analyses for femoral shaft BMD.** Multivariable regression was done using femoral shaft BMD
835 as the dependent variable; explanatory covariables were selected, models constructed, and data presented as described for Table
836 4.

837

838 **FIGURE LEGENDS**

839

840 **Figure 1 – Workflow for data management, manual segmentation and**
841 **application and validation of deep learning.** The test dataset comprised the
842 validation cohort of 729 subjects (described in Table 1), from which datasets from 75
843 subjects were manually segmented (A) to generate four VOIs per subject (spine,
844 femoral head, total hip, and femoral diaphysis). The manual segmentations from 61-
845 64 of these subjects were used to train the deep learning models for each VOI (B),
846 while those from 10-12 subjects were kept as ‘unseen’ segmentations that had not
847 been used to train the models (C). The models were then used to segment all datasets
848 from the 729-subject cohort (D), with deep learning segmentations from the 10-
849 152 validation datasets then compared to the corresponding manual segmentations to
850 calculate dice coefficients for each model (E). Finally, FF maps were generated from
851 each MRI dataset (F) and the deep learning segmentations applied to these to obtain
852 the BMFF for each VOI (G).

853

854 **Figure 2 – Architecture of our CBAM Attention ROI U-Net for segmenting small**
855 **structures from large 3D data.** Each convolutional block in the U-Net encoding
856 subnetwork (or contracting path) includes one or two CBAM (convolutional block
857 attention module) layers. A fixed-size single channel spatial attention map is generated
858 by each CBAM layer through 1X1X1 convolutions and trilinear interpolation. These
859 attention maps are then combined to produce a probability map of object location with
860 which a ROI is defined. The encoded features of all resolution-levels are then cropped
861 to the ROI and input into the decoder which produces the segmentation results within
862 the detected ROI. A non-local spatial attention layer is inserted in the final block to
863 generate globally sensitive features. The final segmentation results are then generated
864 by implanting the ROI back into the whole data volume.

865

866 **Figure 3 – Visual comparison of manual vs deep learning segmentations.** Deep
867 learning segmentation results (purple) are displayed on top of the ground-truth
868 (manual) segmentations (yellow). Representative images from the axial, coronal and
869 sagittal plane are shown, along with a 3D rendering.

870

871 **Figure 4 – Sex differences in BMFF vary according to skeletal region.** BMFF for
872 control subjects was assessed at each skeletal region. Data represent 134 females
873 and 138 males and are shown as violin plots overlaid with individual data points.
874 Significant effects of region, sex, and region*sex interaction were assessed using a
875 mixed-effects model with Šídák’s multiple comparisons test. Overall *P* values for
876 each variable, and their interaction, are shown in the box, while significant sex
877 differences within each region are indicated above.

878

879 **Figure 5 – Osteopaenia or osteoporosis influence BMFF in a sex- and region-**
880 **specific manner.** BMFF for control, osteopaenic and osteoporotic subjects was
881 assessed at each skeletal region. Data are shown as violin plots overlaid with
882 individual data points. Within each sex, significant differences between control and
883 osteopaenic or osteoporotic subjects were assessed by one-way ANOVA (for normally
884 distributed data: A) or the Kruskal-Wallis test (for non-normally distributed data: B-D).
885 *P* values for each comparison are shown on each graph.

Figure 1

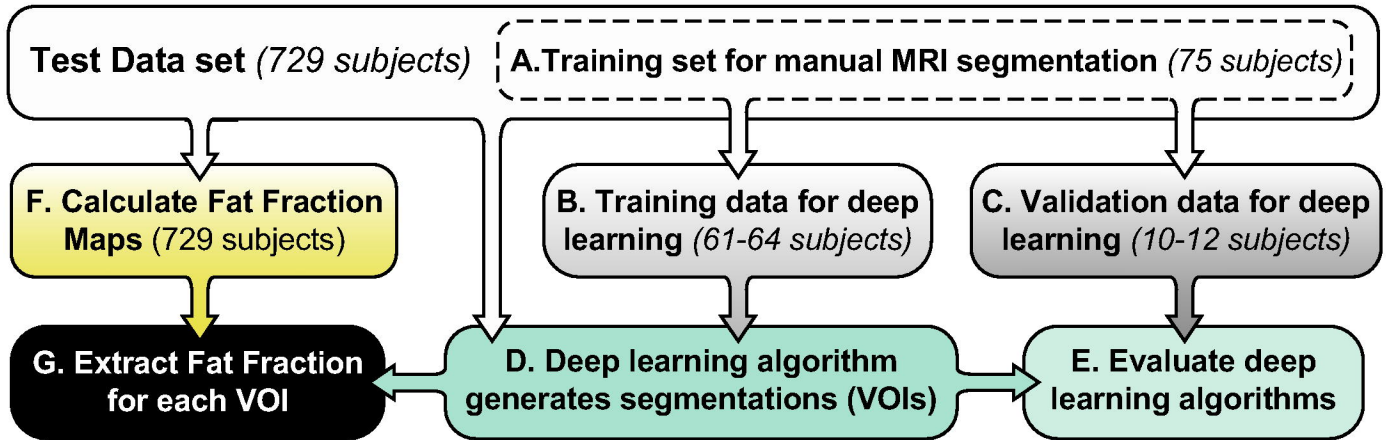


Figure 2

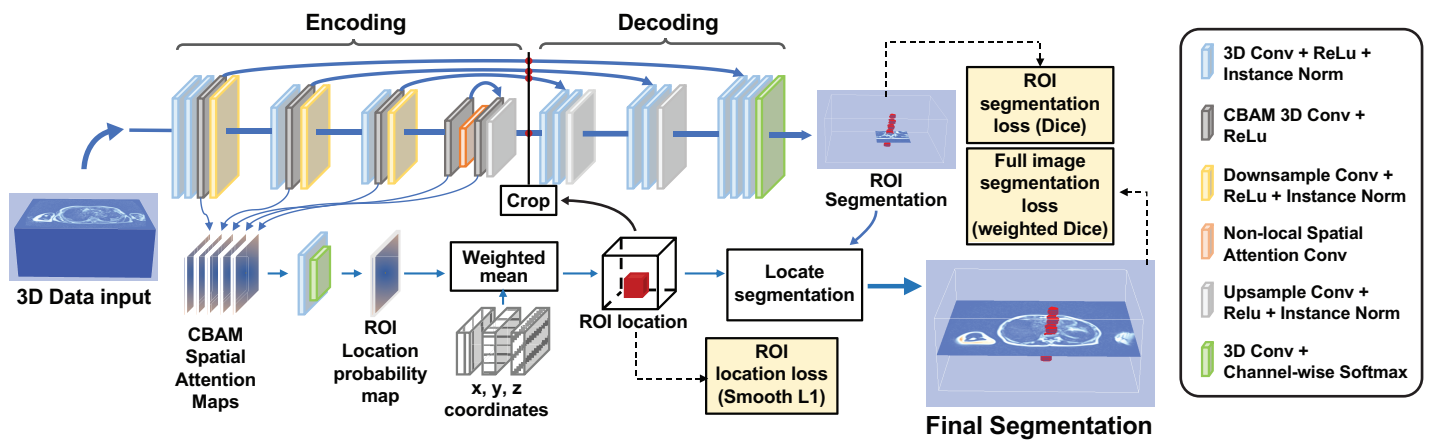


Figure 3

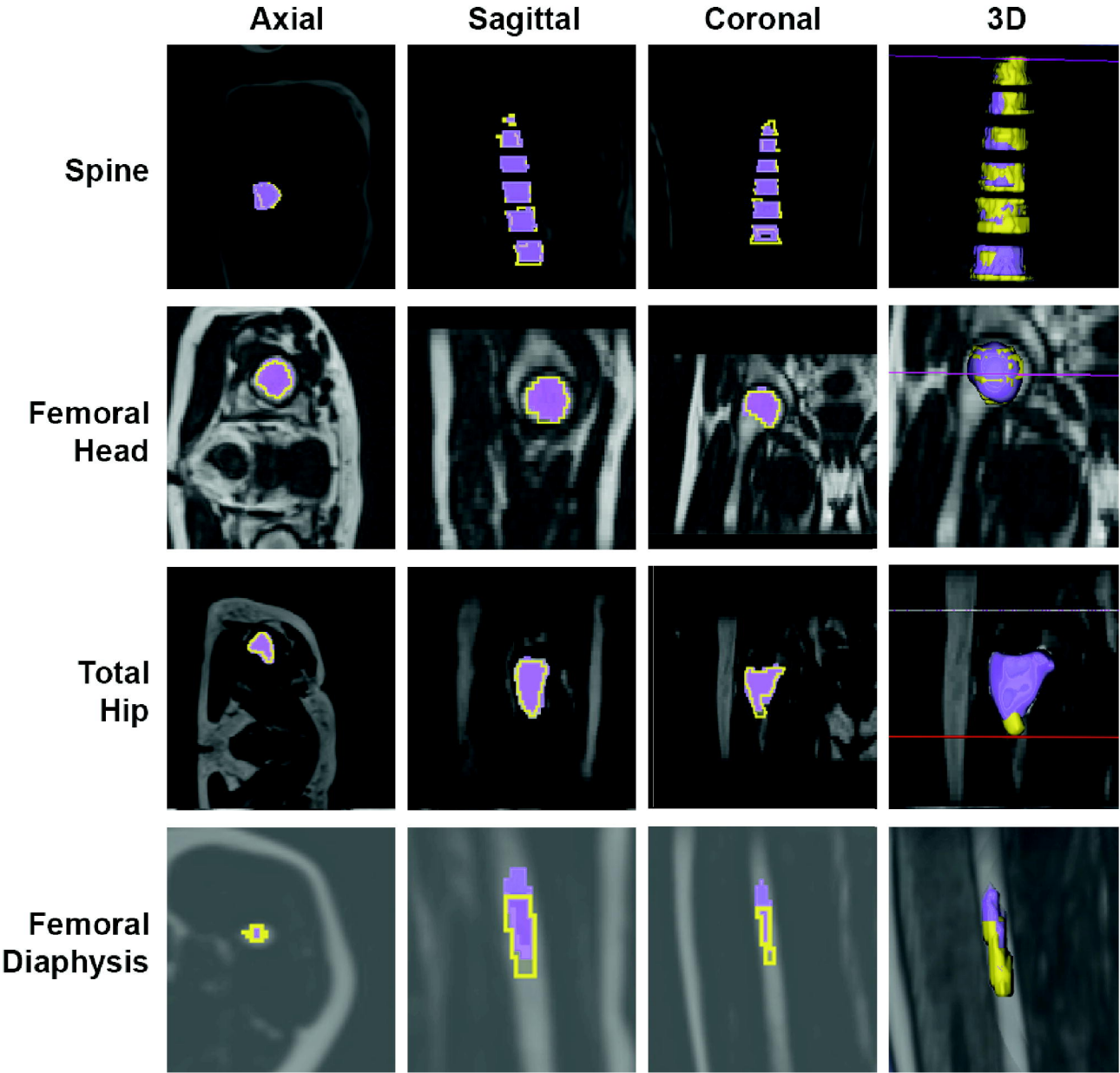


Figure 4

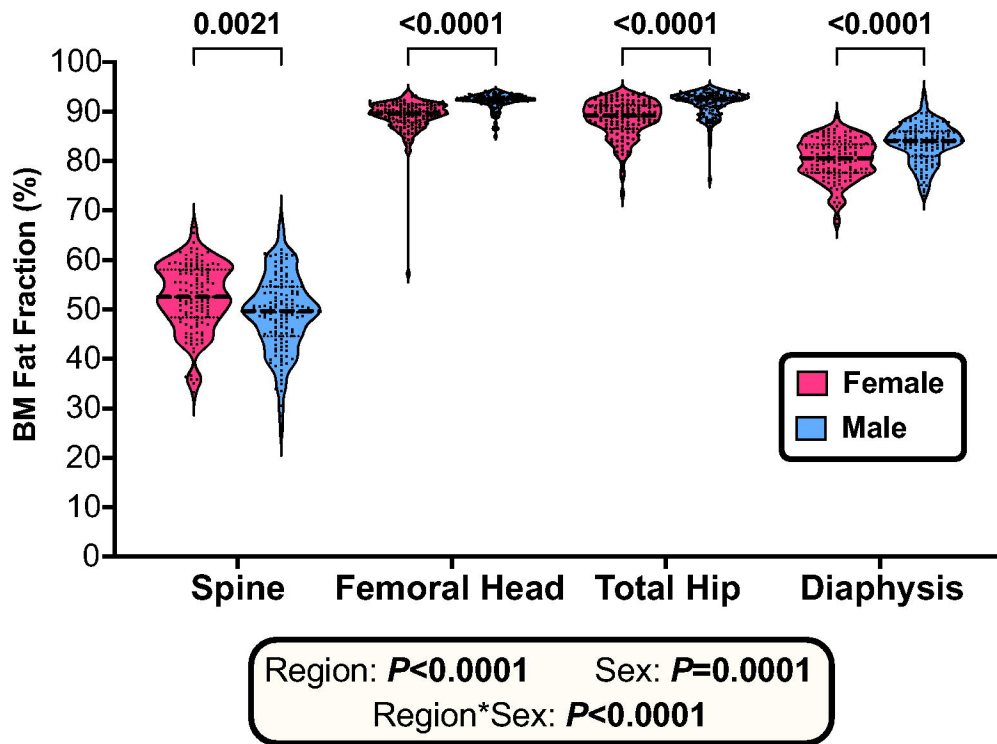


Figure 5

